A Node Role Dynamic Change Method Among Repeater, Receiver, and Decoupling Using Topology Switching in Multinode WPT System

Jinde Wu, Xin Dai, *Member, IEEE*, Yue Sun, *Member, IEEE*, and Yanling Li

***Abstract*—In the multidevice application of wireless power transfer (WPT) technology, classical method cannot balance power transfer efficiency, transfer distance, and dynamic power variation requirements. For multinode WPT system, this article proposes a flexible repeater power transmission mode characterized by node role change function. Each node role can be flexibly switched among repeater, receiver, and decoupling by using a topology switching method to satisfy dynamical repeater power transmission requirements, which is realized by a reusing topology and without additional circuit. Furthermore, the topology switching method is studied to verify that the transition is smooth in dynamic switching. Besides, this article also analyzes the system performances in different operation modes. The experimental results verify the effectiveness of the proposed method.**

***Index Terms*—Multiple nodes, topology switching, wireless power transfer (WPT).**

I. Introduction

OWING to the advantages in convenience, safety, and flexibility, wireless power transfer (WPT) technology has been widely used in household appliances [1]–[3], consumer electronics [4]–[8], electric vehicles [9]–[11], kitchen appliances [12], and etc.

For group robot wireless charging, each robot requires charging frequently and randomly, so the WPT system needs to deal with frequent change among charging, disconnecting, and repeater mode. The multinode WPT mode is an effective solution for the above problems. A wireless power transfer route with multiple wireless power devices is set up, in which each device can work as repeater node, receiver node, or decoupling node. The node role can be changed flexibly according to its status. This method will increase flexibility in group device charging and help to set up a more reliable wireless power route to extend effective wireless power transmission distance.

There are some relevant papers about wireless power transmission through the repeaters. Generally, the repeaters can be added between the transmitter and the receiver to extend the transmission distance, enhance the transfer power and efficiency, and improve the system performance [13]–[16]. In addition, the repeaters added in the system can also improve the position flexibility [17] and achieve the constant output current [18]. The domino WPT system with coaxial and noncoaxial axes is also studied. An optimization method with more than one power flow path is proposed through analyzing the noncoaxial domino WPT system [19]–[20]. To improve the efficiency of the system, the mathematical expression for the power transfer efficiency with an optimal load is derived, and the effects of the varying repeater numbers on the power transfer efficiency are analyzed [21]. It also confirms that there is an optimal repeater number for maximizing the achievable power transfer efficiency for a given end-to-end distance. Furthermore, compared with conventional two-coil-based WPT systems, WPT systems with an intermediate repeater can achieve higher stability of the power transfer efficiency [22]. A computational method proposed in [23], [24] only uses the input voltage and current to identify the impedances of multiple loads in WPT systems without any direct load measurements. The method has been practically realized in a wireless power domino-resonator system comprising eight resonators. From papers [14]–[24], because LC series topology is adopted in each repeater, the stability of the output characteristic will be reduced if the power is transferred to multiple loads. A multifrequency WPT system is described in which the power can be transferred through the wireless power transfer channel [25]. The power can be transferred from the transmitter to the targeted loads with receiver coils specifically tuned for energy reception. A practical implementation of energy harvesting for online monitoring devices on the high-voltage transmission line is achieved by a domino WPT method [26]. It also studies the frequency response of the domino-resonator WPT system and the influence of corona rings installation. Furthermore, the experimental results confirm the feasibility and practicability of the system. In this special application, extending the power transmission distance is the main objective. However, multiple power outputs shorten the distance. The above researches mainly focus on extending the power transmission distance and enhancing the power transfer efficiency by adding

Manuscript received December 6, 2020; revised February 25, 2021; accepted April 1, 2021. Date of publication April 9, 2021; date of current version June 30, 2021. This work was supported in part by the research funds for the National Natural Science Foundation of China under Grants 51777022 and 62073047, and in part by the China National Center for International Research on Wireless Power Transfer Technologies. Recommended for publication by Associate Editor J. Itoh. *(Corresponding author: Xin Dai.)*

Jinde Wu, Xin Dai, and Yue Sun are with the School of Automation, Chongqing University, Chongqing 400044, China (e-mail: 376492330@qq.com; toybear@vip.sina.com; syue06@cqu.edu.cn).

Yanling Li is with the School of Electrical Engineering and Electronic Information, Xihua University, Chengdu 610039, China (e-mail: 57545725@qq.com).

Color versions of one or more figures in this article are available at https://doi.org/10.1109/TPEL.2021.3072203.

Digital Object Identifier 10.1109/TPEL.2021.3072203

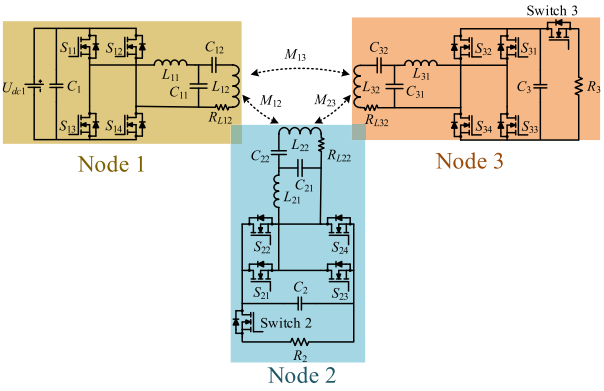

Fig. 1. Proposed multinode WPT system.

multiple repeaters in the system. However, there is only one load in the above systems, so it cannot satisfy the requirement of power supply for multiple devices. Furthermore, different power requirements of the device have not been taken into account.

A WPT system with multiple repeaters is proposed in the article [27]. Every two bipolar coils form a repeater unit where one receives power from its preceding unit and the other transmits power to the subsequent unit. Each load is connected to each repeater, and the load currents are independent of the loads. This special design requires two independent coils for transmitter and receiver and the coils should be placed with a relative fixed placement, which limits its application in some flexible placement environment.

In order to satisfy power transmission among multiple devices (nodes), this article proposes a flexible wireless power transmission mode. In this mode, each node has three operation roles including repeater, receiver, and decoupling, and the node operation roles can be changed dynamically to meet different transmission routes and power requirements. To simplify node structure, a single coil node topology is proposed and role changing function is implemented by a topology switching method. Furthermore, this article utilizes active rectifier method to regulate output voltages.

II. Proposed Multinode WPT System

The proposed WPT system is composed of multiple electronic devices (nodes) with wireless power transfer capability. The power can be transferred through the routes that are built among the devices. In order to satisfy different power transmission requirements, the nodes can be divided as follows:

1) power source node;
2) repeater node;
3) receiver node;
4) decoupling node.

A system with three nodes is taken as an example to study the proposed multinode WPT system. The schematic diagram is shown in Fig. 1. Node 1 is connected to the power grid, while Nodes 2 and 3 are electronic devices. In the system, because the distance between Nodes 1 and 3 is far, the magnetic field between them is quite weak, and the mutual inductance is quite small. Therefore, it is necessary to transfer power from Node 1 to Node 3 through Node 2. Note that the mutual inductance M_{13} between Nodes 1 and 3 is small, so it is neglected in the following studies.

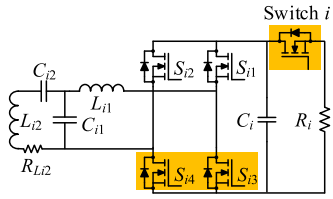

Fig. 2. Topology switching model.

To analyze the system, some basic definitions are given as follows. Each node is composed of full-bridge converter (S_{i1}–S_{i4}), resonant network (L_{i1}–C_{i1}–C_{i2}–L_{i2}), and power source (U_{dc1}) or load (R_i) ($i = 2, 3$). The resistance of each coil is expressed as R_{Li2}, and the equivalent ac impedance before the rectifier is expressed as R_{li} ($i = 2, 3$). The operation frequency of the inverter in power source node is f, its angular frequency is ω ($\omega = 2\pi f$), and U_{ac1} is the output voltage of the inverter in Node 1.

In the designed topology, when the capacitances and inductances of each node satisfy (1) and (2), the equivalent impedances of each node exhibit resistive:

$$\omega^2 = \frac{1}{L_{i1}C_{i1}} = \frac{1}{L_iC_{i1}} (i = 1, 2, 3) \tag{1}$$

where

$$\frac{1}{j\omega C_{i2}} + j\omega L_{i2} = j\omega L_i. \tag{2}$$

In order to achieve different objectives of power transmission, each node can switch its role according to the status of each node and the specific power transmission demand. When a node is in different operation states, its topology switches accordingly, and the topology switching model is shown in Fig. 2.

When Switch i is turned OFF, the node is a L_{i2}–C_{i1}–C_{i2} topology in series. According to (1) and (2), the node is still in resonant state. When S_{i3} and S_{i4} of the converter are turned ON, the load is short-circuited. The simplified circuits, node states, output voltages, and transfer efficiency in different operation modes are listed in Table I.

III. Switching Method of the Operation Modes

The topology of each node is switched dynamically with different roles and operation modes of the system. The node role determining method is shown in Fig. 3.

The following part focuses on the dynamic switching of Node 2 from repeater and receiver node to repeater node and Node 3 from receiver node to decoupling node, that is, Nodes 2 and 3 switch from the state with power supply to the other state without power supply, respectively. In other words, the system dynamically switches from Mode 3 to 1 and from Mode 3 to 2.

TABLE I
SIMPLIFIED CIRCUITS, NODE STATES, OUTPUT VOLTAGES, AND TRANSFER EFFICIENCY IN DIFFERENT OPERATION MODES

	Simplified circuit	Node 1	Node 2	Node 3
Mode 1	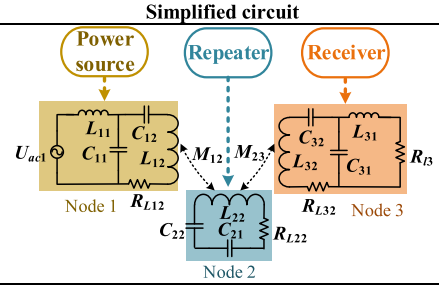	Power source node	Repeater node Does not require power S_{23} and S_{24}: "OFF" Switch 2: "OFF"	Receiver node Requires power S_{33} and S_{34}: "OFF" Switch 3: "ON"
		Output voltage	$U_{o3}=\frac{U_{ac1}\omega^2 M_{12}M_{23}L_3}{L_1\left(\frac{\omega^2 M_{23}^2 R_{l3}}{(\omega L_3)^2+R_{l3}R_{L32}}+R_{L22}\right)\left(\frac{(\omega L_3)^2}{R_{l3}}+R_{L32}\right)}$	
		Efficiency	$\eta=\frac{P_{out\_3}}{P_{in}}$	
	Simplified circuit	**Node 1**	**Node 2**	**Node 3**
Mode 2	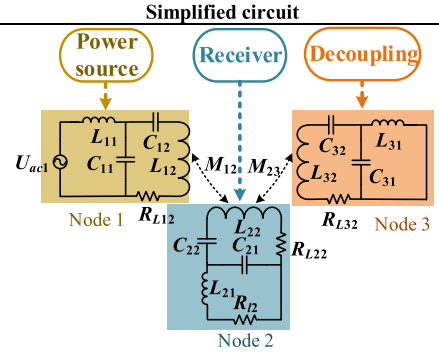	Power source node	Receiver node Requires power S_{23} and S_{24}: "OFF" Switch 2: "ON"	Decoupling node Does not require power S_{33} and S_{34}: "ON" Switch 3: "ON"
		Output voltage	$U_{o2}=\frac{U_{ac1}\omega M_{12}L_2R_{l2}}{L_1\left((\omega L_2)^2+R_{l2}R_{L22}\right)}$	
		Efficiency	$\eta=\frac{P_{out\_2}}{P_{in}}$	
	Simplified circuit	**Node 1**	**Node 2**	**Node 3**
Mode 3	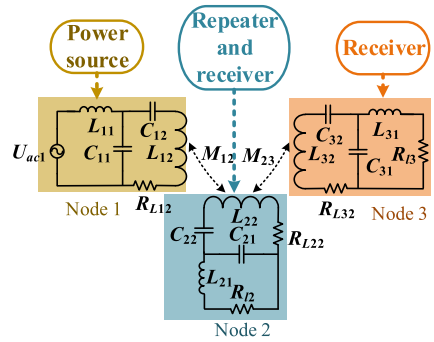	Power source node	Repeater and receiver node Requires power S_{23} and S_{24}: "OFF" Switch 2: "ON"	Receiver node Requires power S_{33} and S_{34}: "OFF" Switch 3: "ON"
		Output voltages	$U_{o2}=\frac{U_{ac1}\omega M_{12}L_2}{L_1\left(\frac{(\omega L_2)^2}{R_{l2}}+\frac{(\omega M_{23})^2 R_{l3}}{(\omega L_3)^2+R_{l3}R_{L32}}+R_{L22}\right)}$ $U_{o3}=\frac{U_{ac1}\omega^2 M_{12}M_{23}L_3}{L_1\left(\frac{(\omega L_2)^2}{R_{l2}}+\frac{(\omega M_{23})^2 R_{l3}}{(\omega L_3)^2+R_{l3}R_{L32}}+R_{L22}\right)\left(\frac{(\omega L_3)^2}{R_{l3}}+R_{L32}\right)}$	
		Efficiency	$\eta=\frac{P_{out\_2}+P_{out\_3}}{P_{in}}$	

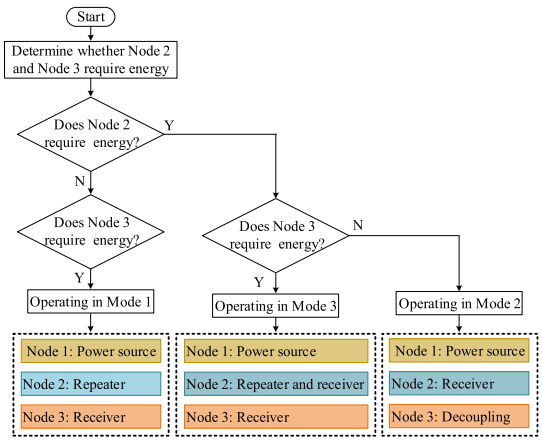

Fig. 3. Node role determining method.

A. Switching From Mode 3 to 1

When Switch 2 of Node 2 is turned OFF, the system switches from Mode 3 to 1, and Node 2 switches from repeater and receiver node to repeater node.

When the system works in Mode 3, the current I_{L22} in the coil L_{22} can be expressed as

$$I_{L22\_Mode\_3}=\frac{U_{ac1}M_{12}}{L_1\left(\frac{\omega^2 M_{23}^2 R_{l3}}{\omega^2 L_3^2+R_{L32}R_{l3}}+\frac{\omega^2 L_2^2+R_{L22}R_{l2}}{R_{l2}}\right)}. \quad (3)$$

When the system switches from Mode 3 to 1, Switch 2 is turned OFF, then in Mode 1, I_{L22} can be expressed as

$$I_{L22\_Mode\_1}=\frac{U_{ac1}M_{12}}{L_1\left(\frac{\omega^2 M_{23}^2 R_{l3}}{\omega^2 L_3^2+R_{L32}R_{l3}}+R_{L22}\right)}. \quad (4)$$

It can be seen that the current I_{L22} in Mode 1 increases compared to that in Mode 3. When the system switches from Mode 3 to 1, the voltage and current variations of each node are shown in Fig. 4(a). u_{ac1} is the output voltage of the inverter in Node 1, i_{L21} and i_{L22} are the currents of L_{21} and L_{22}, respectively. u_{out_2} and u_{out_3} are the output voltages of Nodes 2 and 3, respectively. According to the simulation results, the transient variations of current i_{L21} and i_{L22} are shown in Fig. 4(b) when Switch 2 is turned OFF and they are shown in Fig. 4(c) when Switch 2 is turned ON.

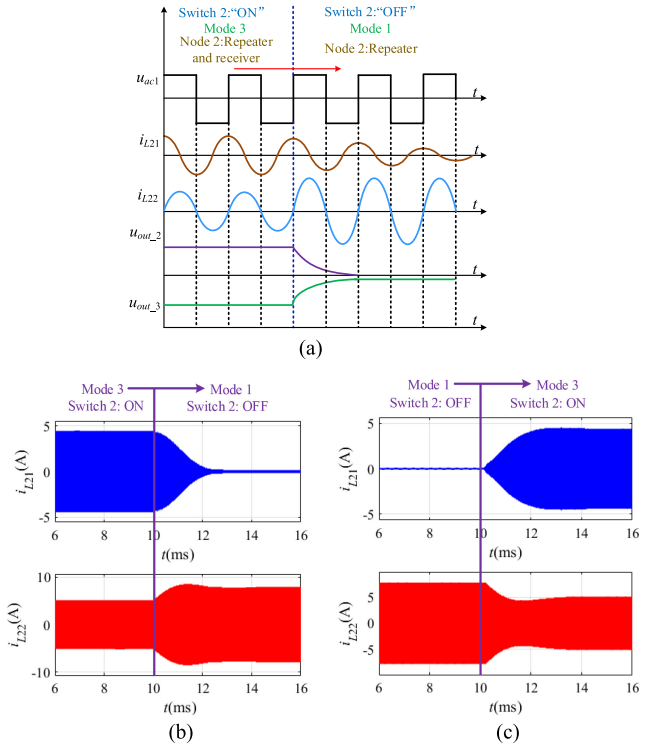

Fig. 4. Voltage and current variations of each node when the system switches from Mode 3 to 1. (a) Voltage and current variations of each node. (b) Transient variations of current i_{L21} and i_{L22} when Switch 2 is turned OFF. (c) Transient variations of current i_{L21} and i_{L22} when Switch 2 is turned ON.

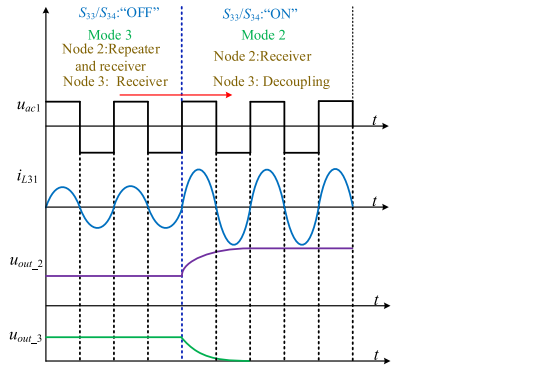

Fig. 5. Voltage and current variations of each node when the system switches from Mode 3 to 2.

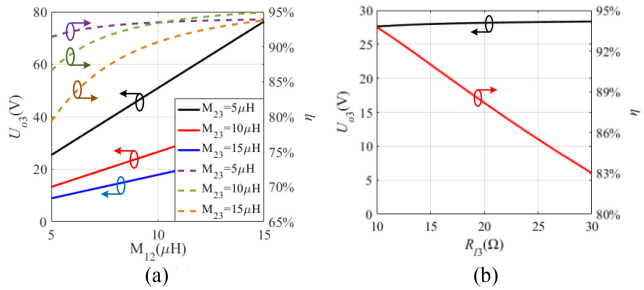

Fig. 6. Variations of the output voltage U_{o3} and the efficiency η in Mode 1 with the mutual inductances and load. (a) Variations of U_{o3} and η with the mutual inductances. (b) Variations of U_{o3} and η with the load.

As can be seen from Fig. 4(a), when Switch 2 is turned OFF, the output voltage of Node 2 $u_{\mathrm{out\_2}}$ decreases to 0, the output voltage of Node 3 $u_{\mathrm{out\_3}}$ increases, the current i_{L21} decreases to 0, and the current i_{L22} increases. It can be seen from Fig. 4(b) and (c) that the transition is smooth when Switch 2 is turned OFF and turned ON.

B. Switching From Mode 3 to Mode 2

When S_{33} and S_{34} of the converter in Node 3 are turned ON, the system switches from Mode 3 to 2, and Node 3 switches from receiver node to decoupling node. The following part focuses on the voltage and current variations of each node when S_{33} and S_{34} are turned ON. The current of L_{31} is marked as I_{L31}, which is also the current in the converter switching components. When the system works in Mode 3, I_{L31} can be expressed as

$$I_{L31\_Mode\_3} = \frac{U_{\mathrm{ac1}} M_{12} M_{23}}{L_1 L_3 \left(\frac{\omega^2 M_{23}^2 R_{l3}}{\omega^2 L_3^2 + R_{L32} R_{l3}} + \frac{\omega^2 L_2^2 + R_{L22} R_{l2}}{R_{l2}} \right)}. \tag{5}$$

When the system switches from Mode 3 to 2, S_{33} and S_{34} are turned ON, the load branch is short-circuited, and R_{l3} decreases to 0, then in Mode 2, I_{L31} can be expressed as

$$I_{L31\_Mode\_2} = \frac{U_{\mathrm{ac1}} M_{12} M_{23} R_{l2}}{L_1 L_3 \left(\omega^2 L_2^2 + R_{L22} R_{l2} \right)}. \tag{6}$$

It can be seen that the current I_{L31} in Mode 2 increases compared to that in Mode 3. The voltage and current variations of each node are shown in Fig. 5.

Fig. 5 shows the voltage and current variations of each node when the system switches from Mode 3 to 2. When S_{33} and S_{34} are turned ON, the output voltage of Node 2 $u_{\mathrm{out\_2}}$ increases, the output voltage of Node 3 $u_{\mathrm{out\_3}}$ decreases to 0, and the current i_{L31} increases.

From the above analyses, it can be seen that the topology switching model, as shown in Fig. 2, cannot only satisfy the requirements of different operation modes, but also achieve a smooth transition when the topology is switched dynamically.

IV. Performance Analysis

A. Mode 1

When the system works in Mode 1, if the coil resistance is neglected, the output voltage U_{o3} of Node 3 can be expressed as

$$U_{o3} = \frac{U_{\mathrm{ac1}} M_{12} L_3}{L_1 M_{23}}. \tag{7}$$

The variations of the output voltage U_{o3} and the efficiency η in Mode 1 with the mutual inductances and load are shown in Fig. 6.

It can be seen from Fig. 6(a) that when M_{12} and M_{23} increase from 5 to 15 μH, the output voltage U_{o3} varies from 10 to 75 V, and the efficiency η varies from 80% to 95%. From Fig. 6(b), when R_{l3} increases from 10 to 30 Ω, U_{o3} increases from 28.5 to 29.1 V, and η decreases from 93% to 83.5%. It can be seen from the above analyses that U_{o3} increases with the increase of M_{12}

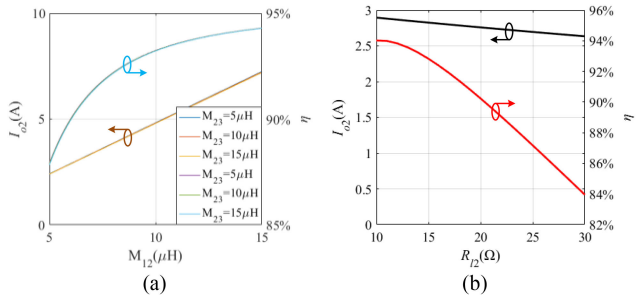

Fig. 7. Variations of output current I_{o2} and efficiency η in Mode 2 with the mutual inductances and load. (a) Variations of I_{o2} and η with the mutual inductances. (b) Variations of I_{o2} and η with the load.

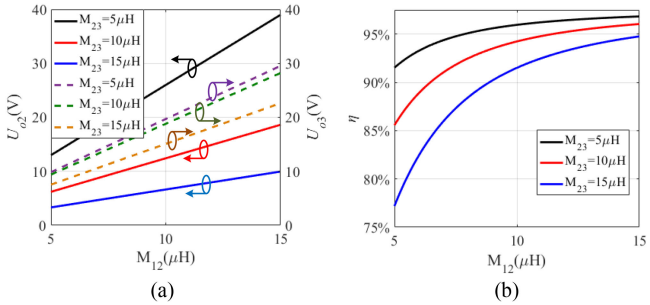

Fig. 8. Variations of the output voltages (U_{o2} and U_{o3}) and efficiency η in Mode 3 with the mutual inductances. (a) Variations of U_{o2} and U_{o3} with the mutual inductances. (b) Variation of η with the mutual inductances.

and decreases with the increase of M_{23}, and U_{o3} is not sensitive to the variation of R_{l3}, which is consistent with (7).

B. Mode 2

When the system works in Mode 2, if the coil resistance is neglected, the output current I_{o2} of Node 2 can be expressed as

$$I_{o2} = \frac{U_{\mathrm{ac1}} M_{12}}{\omega L_1 L_2}. \tag{8}$$

The variations of output current I_{o2} and efficiency η in Mode 2 with the mutual inductances and load are shown in Fig. 7.

It can be seen from Fig. 7(a) that when M_{12} and M_{23} increase from 5 to 15 μH, the output current I_{o2} increases from 2.3 to 6.7 A, and the efficiency η increases from 87.5% to 94.3%. From Fig. 7(b), when R_{l2} increases from 10 to 30 Ω, I_{o2} decreases from 2.9 to 2.7 A, and η decreases from 94.1% to 83.8%. It can be seen from the above analyses that I_{o2} increases with the increase of M_{12}, and I_{o2} is not sensitive to the variations of M_{23} and R_{l2}, which is consistent with (8).

C. Mode 3

When the system works in Mode 3, the variations of the output voltages U_{o2} and U_{o3}, and the efficiency η with the mutual inductances are shown in Fig. 8.

As can be seen from Fig. 8(a), when R_{l2} and R_{l3} are fixed at 10 Ω and M_{12} and M_{23} increase from 5 to 15 μH, the output voltage U_{o2} varies from 3.3 to 39.2 V, U_{o3} varies from 7.6 to 30.5 V. As can be seen from Fig. 8(b), the efficiency η varies from 77.2% to 96.8%.

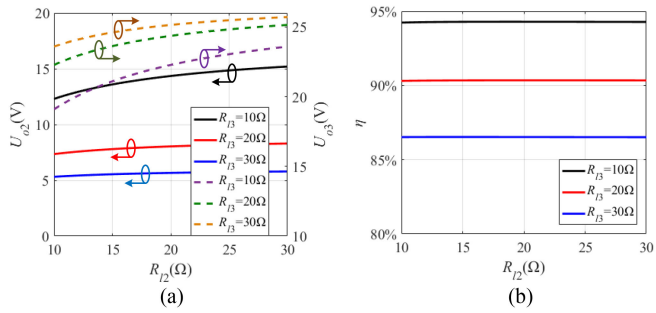

Fig. 9. Variations of the output voltages (U_{o2} and U_{o3}) and the efficiency η in Mode 3 with the loads. (a) Variations of U_{o2} and U_{o3} with the loads. (b) Variation of η with the loads.

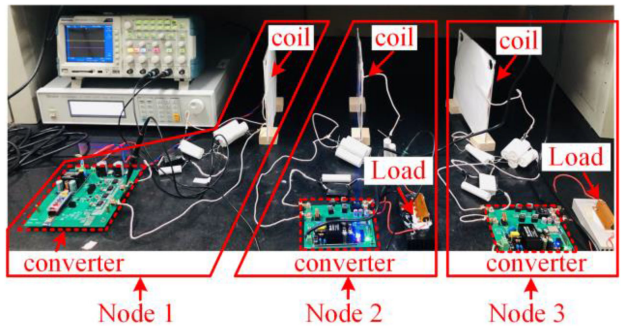

Fig. 10. Experimental platform.

TABLE II
EXPERIMENTAL PARAMETERS

Parameter	Value	Parameter	Value
L_{11}	9.2 μH	C_{11}	275.3 nF
C_{12}	35.3 nF	L_{12}	80.9 μH
R_{L12}	0.15 Ω	L_{21}	9.2 μH
C_{21}	275.5 nF	C_{22}	35.1 nF
L_{22}	81 μH	R_{L22}	0.16 Ω
L_{31}	9.2 μH	C_{31}	275.4 nF
C_{32}	35.5 nF	L_{32}	80.5 μH
R_{L32}	0.15 Ω	f	100 KHz

The variations of the output voltages (U_{o2} and U_{o3}) and the efficiency η in Mode 3 with the loads are shown in Fig. 9.

As can be seen from Fig. 9 (a), when M_{12} and M_{23} are fixed at 10 μH and R_{l2} and R_{l3} increase from 10 to 30 Ω, the output voltage U_{o2} varies from 5.3 to 15.2 V, U_{o3} varies from 19 to 25.7 V. As can be seen from Fig. 9(b), the efficiency η varies from 86.5% to 94.2%.

V. EXPERIMENTAL VERIFICATION

In order to verify the proposed method, an experimental platform shown in Fig. 10 is set up. The system consists of three nodes: Node 1, Node 2, and Node 3. *LCCL* topology is adopted in each node. Each node coil is disc structure with a diameter of 200 mm. Furthermore, MOSFET is selected as the switching component of the converter. The roles of the node are changed through switching the topology. Furthermore, Mode 3 is taken as an example to show the method of the output voltage adjustment. The experimental parameters are shown in Table II.

The validity of the theory and the feasibility of the proposed system are verified from the following aspects:

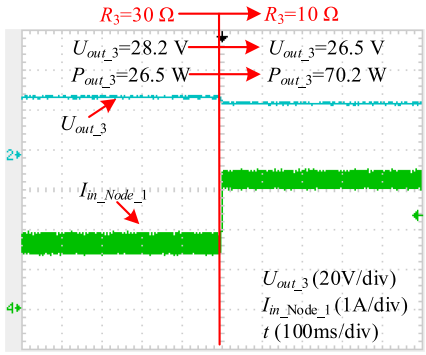

Fig. 11. Influence of load variation on output voltage in Mode 1.

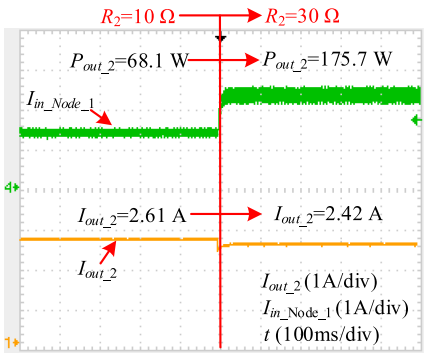

Fig. 12. Influence of load variation on output current in Mode 2.

1) the influence of load variation on output voltage in Mode 1;
2) the influence of load variation on output current in Mode 2;
3) the adjustment of the output voltages in Mode 3;
4) dynamic switching from Mode 3 to 1 and then to Mode 2;
5) output voltage stability regulation under the variations of loads, mutual inductances, and operation modes.

A. Mode 1

Fig. 11 shows the influence of load variation on the output voltage in Mode 1. $U_{\text{out\_3}}$ is the output voltage of Node 3, $I_{\text{in\_Node\_1}}$ is the input current of Node 1. In Mode 1, when the load R_3 decreases from 30 to 10 Ω, the output voltage $U_{\text{out\_3}}$ decreases from 28.2 to 26.5 V, $\Delta U_{\text{out\_3}} = 1.7$ V, the change ratio is $\delta = 2\Delta U_{\text{out\_3}} / (28.2 + 26.5) = 6.2\%$, and the output power $P_{\text{out\_3}}$ increases from 26.5 to 70.2 W. According to (7), the output voltage is not sensitive to the variation of the load, and the experimental result is consistent with the theory. With the decrease of the load, the output power increases, the input power increases with the increase of the output power, and $I_{\text{in\_Node\_1}}$ increases accordingly.

B. Mode 2

Fig. 12 shows the influence of load variation on the output current in Mode 2. $I_{\text{out\_2}}$ is the output current of Node 2. In Mode 2, when the load R_2 increases from 10 to 30 Ω, the output current $I_{\text{out\_2}}$ decreases from 2.61 to 2.42 A, $\Delta I_{\text{out\_2}} = 0.19$ A, the change ratio is $\delta = 2\Delta I_{\text{out\_2}} / (2.61 + 2.42) = 7.6\%$, and the output power $P_{\text{out\_2}}$ increases from 68.1 to 175.7 W. According to (8), the output current is not sensitive to the variation of load, and the experimental result is consistent with the theory. With the increase of the load, the output power increases, the input power increases with the increase of the output power, and then $I_{\text{in\_Node\_1}}$ increases accordingly.

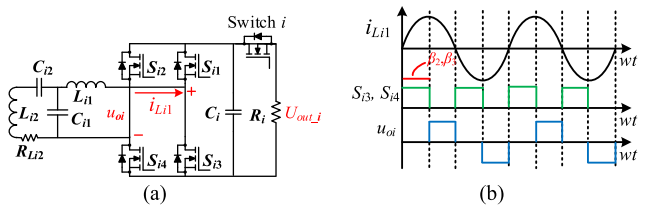

Fig. 13. Active rectifier and operation waveform. (a) Circuit diagram of active rectifier. (b) Operation waveform.

C. Mode 3

In application, the output voltage of each node usually needs to be adjusted to satisfy the actual voltage demand. Therefore, Mode 3 is taken as an example to show the method of the output voltage adjustment, and the method can also be applied to Modes 1 and 2.

When the system works in Mode 3, both Node 2 and 3 need power. The output voltage of each node can be adjusted through the active rectification of Node 2 and 3. The conduction angles of Node 2 and Node 3 converters are defined as β_2 and β_3, respectively.

The circuit diagram of active rectifier in Node 2 and 3 and operation waveform are shown in Fig. 13.

The relationship between the output voltage $U_{\text{out}\cdot i}$ and the voltage $U_{o(i)}$ before rectifier is

$$U_{o(i)} = \frac{2\sqrt{2}}{\pi} U_{\text{out\_}i} \cos\frac{\beta_i}{2}. (0 \le \beta_i < \pi) (i = 2, 3). \quad (9)$$

Then, the relationship between the load R_i and equivalent ac impedance before rectifier R_{li} can be expressed as

$$R_{li} = \frac{8R_i}{\pi^2} \cos^2\frac{\beta_i}{2}. (0 \le \beta_i < \pi) (i = 2, 3). \quad (10)$$

The experimental results of the output voltage adjustment are as follows.

In Mode 3, the adjustment of the output voltages under different mutual inductances is shown in Fig. 14. U_{o2} and U_{o3} are the voltages before the rectifier of Node 2 and 3, respectively. The loads of Node 2 and Node 3 are 10 Ω, respectively. The reference output voltages of Node 2 and Node 3 are defined as $U_{\text{out\_2\_ref}} = 23$ V, $U_{\text{out\_3\_ref}} = 17$ V, respectively. When $M_{12} = 10.5$ μH, $M_{23} = 4.5$ μH, $\beta_2 = 18°$, $\beta_3 = 51°$, the output voltages are $U_{\text{out\_2}} = 23.1$ V, $U_{\text{out\_3}} = 17.4$ V, and the output powers are $P_{\text{out\_2}} = 53.4$ W, $P_{\text{out\_3}} = 30.3$ W. When $M_{12} = 6.57$ μH, $M_{23} = 7.25$ μH, $\beta_2 = 72°$, $\beta_3 = 58°$, the output voltages are $U_{\text{out\_2}} = 22.9$ V, $U_{\text{out\_3}} = 17.8$ V, the output powers are $P_{\text{out\_2}} = 52.4$ W, $P_{\text{out\_3}} = 31.7$ W. When $M_{12} = 4.2$ μH, $M_{23} = 11.58$ μH, $\beta_2 = 108°$, $\beta_3 = 75°$, the output voltages are $U_{\text{out\_2}} = 22.6$ V, $U_{\text{out\_3}} = 17.7$ V, and the output powers are $P_{\text{out\_2}} = 51.1$ W,

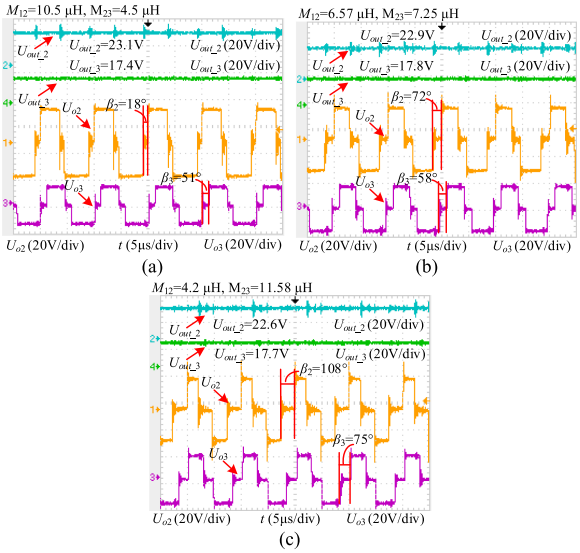

Fig. 14. Output voltage adjustment under different mutual inductances. (a) $M_{12} = 10.5\ \mu$H, $M_{23} = 4.5\ \mu$H. (b) $M_{12} = 6.57\ \mu$H, $M_{23} = 7.25\ \mu$H. (c) $M_{12} = 4.2\ \mu$H, $M_{23} = 11.58\ \mu$H.

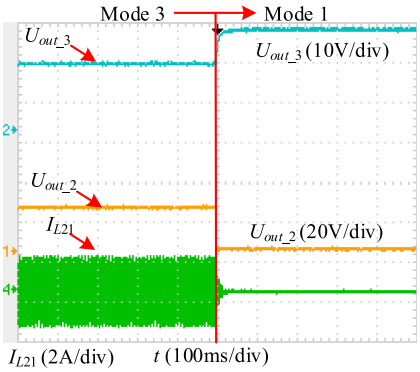

Fig. 15. Operation mode switching from Mode 3 to 1.

$P_{\text{out\_3}} = 31.3$ W. It can be seen that the voltage demand of each node can be satisfied under different mutual inductances.

D. Dynamic Switching

The operation mode switching from Mode 3 to Mode 1 is shown in Fig. 15. The loads of Node 2 and Node 3 are 10 Ω, respectively. I_{L21} is the current of inductance L_{21}. When Switch 2 is turned OFF, the output voltage of Node 2 $U_{\text{out\_2}}$ decreases from 22.9 V to 0, the output voltage of Node 3 $U_{\text{out\_3}}$ increases from 17.4 to 25.8 V, and the current I_{L21} decreases to 0. It can be seen from Fig. 15 that the transition is smooth when the system switches from Mode 3 to 1 dynamically.

The operation mode switching from Mode 3 to 2 is shown in Fig. 16. The loads of Node 2 and 3 are 10 Ω. I_{L31} is the current of L_{31}. When S_{33} and S_{34} are turned ON, $U_{\text{out\_2}}$ increases from 23.1 to 31.9 V, $U_{\text{out\_3}}$ decreases from 17.4 V to 0, and I_{L31} increases. It can be seen from Fig. 16 that the transition is smooth when the system switches from Mode 3 to 2 dynamically.

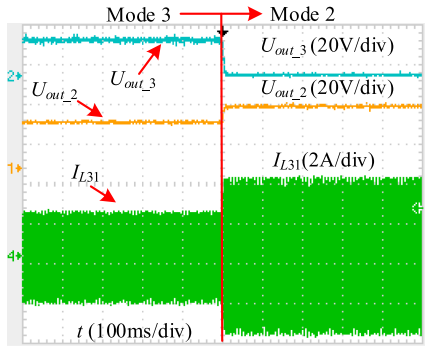

Fig. 16. Operation mode switching from Mode 3 to Mode 2.

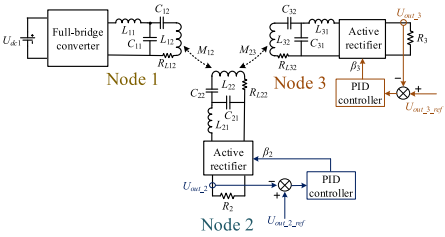

Fig. 17. Control strategy of stable output voltages.

E. Close-Loop Control Strategy for Stable Output Voltages

The control strategy of stable output voltages is shown in Fig. 17. In Nodes 2 and 3, the errors between the reference output voltage values and the actual output voltage values are fed back into PID controllers to generate the conduction angles β_2 and β_3 and subsequent control signals for the active rectifiers, and then maintain the output voltages stable regardless of the variations of loads, mutual inductances, and operation modes.

Fig. 18 shows the output voltage waveforms under load variations in Mode 3. $U_{\text{out\_2}}$ and $U_{\text{out\_3}}$ are the output voltages of Node 2 and 3, S_{23}/S_{24} and S_{33}/S_{34} are the drive signal of the active rectifiers in Node 2 and 3. The reference output voltages of Node 2 and 3 are defined as $U_{\text{out\_2\_ref}} = 20$ V, $U_{\text{out\_3\_ref}} = 20$ V, respectively. It can be seen that $U_{\text{out\_2}}$ and $U_{\text{out\_3}}$ can be maintained steady with a slight overshoot when R_2 and R_3 vary between 10 and 30 Ω. $U_{\text{out\_2}}$ and $U_{\text{out\_3}}$ are almost unchanged and tightly controlled to the reference value with the variations of R_2 and R_3.

Fig. 19(b) shows the output voltage waveforms under the coil position variations in Mode 3. It can be seen that $U_{\text{out\_2}}$ and $U_{\text{out\_3}}$ can be maintained steady with a slight overshoot regardless of the variations of the coil positions.

Fig. 20 shows the output voltage waveforms under the operating mode switching. It can be seen from Fig. 20(a) that when the system switches from Mode 3 to 1, the output voltage of Node 2 $U_{\text{out\_2}}$ decreases from 20.4 V to 0, and the output voltage of Node 3 $U_{\text{out\_3}}$ is maintained steady with a slight overshoot. Similarly, it can be seen from Fig. 20(b) that when the system switches from Mode 3 to 2, the output voltage of Node 3 $U_{\text{out\_3}}$ decreases from 20.8 V to 0, and the output voltage of Node 2 $U_{\text{out\_2}}$ is maintained steady with a slight overshoot. $U_{\text{out\_2}}$

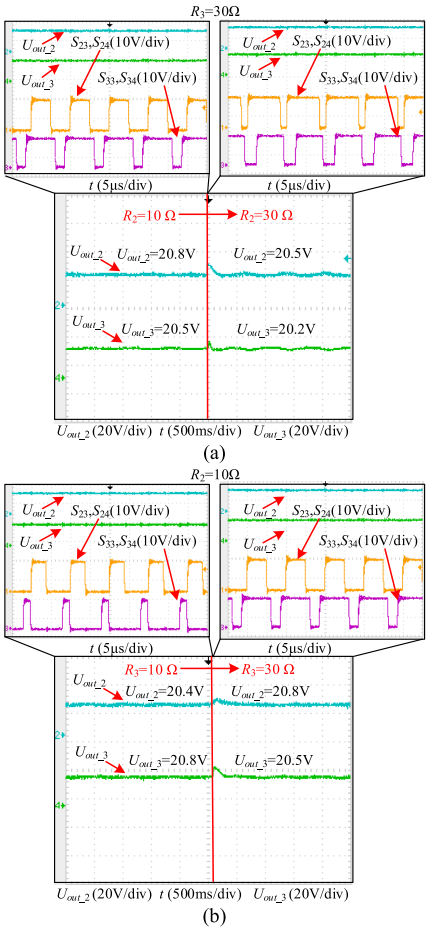

Fig. 18. Output voltage adjustment under load variations in Mode 3. (a) $R_3 = 30\ \Omega$, R_2 varies from 10 to 30 Ω. (b) $R_2 = 10\ \Omega$, R_3 varies from 10 to 30 Ω.

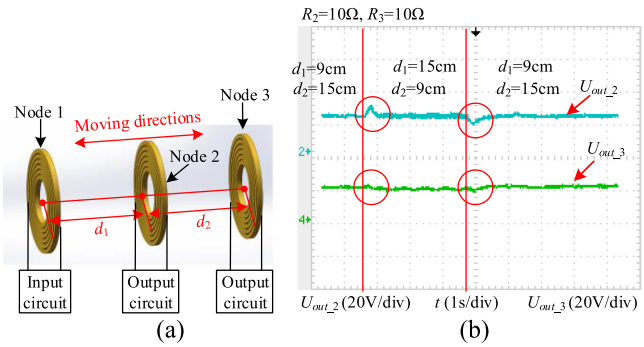

Fig. 19. Output voltage adjustment under the variations of the coil positions in Mode 3. (a) Relative position of three coils. (b) Output voltage waveforms under the coil position variations.

and $U_{\mathrm{out\_3}}$ are almost unchanged and tightly controlled to the reference value under the operating mode switching.

The current researches on WPT systems with multiple repeaters are listed in Table III. Compared with the previous works, the proposed method in this article can satisfy the requirement of charging for multiple electronic devices at the same time. Furthermore, the proposed system can provide flexible operation mode for each device.

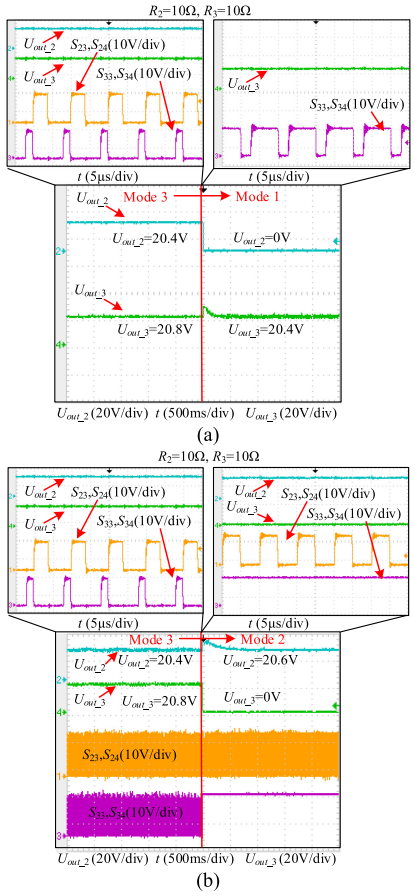

Fig. 20. Output voltage adjustment of the operation mode switching. (a) Operation mode switching from Mode 3 to 1. (b) Operation mode switching from Mode 3 to 2.

TABLE III
COMPARISON OF RECENT WORKS ON WPT SYSTEMS WITH MULTIPLE REPEATERS

Paper	Whether the repeater can output power	Whether the system can provide flexible operation mode	Power level
[11]	NO	NO	<1 W
[14]	NO	NO	1 W
[15]	NO	NO	18 W
[16]	NO	NO	15 W
[17]	NO	NO	14 W
[18]	NO	NO	14 W
[23]	NO	NO	5 W
[24]	NO	NO	6 W
[25]	YES	NO	25 W
[26]	YES	NO	85.92 W
This paper	YES	YES	175.7 W

VI. CONCLUSION

In this article, a flexible wireless power transfer mode is proposed to meet multiple-device power supply requirement. In this mode, all devices (nodes) can easily change its status according to different power requirement and wireless power transmission routes. A simple topology-switching method is also presented to realize this goal. With this method, group device wireless power can be easily achieved and group power transmission performance can be improved because a good balance can be

kept among multiple indexes including total system efficiency and power transmission distance.

REFERENCES

[1] C. Y. Xia, L. Liu, Y. L. Liu, and Z. Ma, "Inductive power transfer system for tail-free household appliances in smart home system," *IET Power Electron.*, vol. 12, no. 5, pp. 1002–1010, Jan. 2019.

[2] J. Chen, S. Li, S. Chen, S. He, and Z. Shi, "Q-charge: A quadcopter-based wireless charging platform for large-scale sensing applications," *IEEE Netw.*, vol. 31, no. 6, pp. 56–61, Nov./Dec. 2017.

[3] D. Kurschner, C. Rathge, and U. Jumar, "Design methodology for high efficient inductive power transfer systems with high coil positioning flexibility," *IEEE Trans. Ind. Electron.*, vol. 60, no. 1, pp. 372–381, Jan. 2013.

[4] M. Liu, C. Zhao, J. Song, and C. Ma, "Battery charging profile-based parameter design of a 6.78-MHz class E^2 wireless charging system," *IEEE Trans. Ind. Electron.*, vol. 64, no. 8, pp. 6169–6178, Aug. 2017.

[5] Y. Li *et al.*, "Extension of ZVS region of series-series WPT systems by an auxiliary variable inductor for improving efficiency," *IEEE Trans. Power Electron.*, vol. 36, no. 7, pp. 7513–7525, Jul. 2021.

[6] W. Zhou, L. Huang, B. Luo, R. Mai, Z. He, and A. P. Hu, "A general mutual coupling model of MIMO capacitive coupling interface with arbitrary number of ports," *IEEE Trans. Power Electron.*, vol. 36, no. 6, pp. 6163–6167, Jun. 2021.

[7] J. Feng, Q. Li, F. Lee, and M. Fu, "Transmitter coils design for free-positioning omnidirectional wireless power transfer system," *IEEE Trans. Ind. Inform.*, vol. 15, no. 8, pp. 4656–4664, Aug. 2019.

[8] Y. Li *et al.*, "Analysis, design and experimental verification of a mixed high order compensations-based WPT system with constant current outputs for driving multistring LEDs," *IEEE Trans. Ind. Electron.*, vol. 67, no. 1, pp. 203–213, Jan. 2020.

[9] Y. Li *et al.*, "A new coil structure and its optimization design with constant output voltage and constant output current for electric vehicle dynamic wireless charging," *IEEE Trans. Ind. Inform.*, vol. 15, no. 9, pp. 5244–5256, Sep. 2019.

[10] X. Dai, X. Li, Y. Li, and A. P. Hu, "Maximum efficiency tracking for wireless power transfer systems with dynamic coupling coefficient estimation," *IEEE Trans. Power Electron.*, vol. 33, no. 6, pp. 5005–5015, Jun. 2018.

[11] X. Dai, J. Jiang, and J. Wu, "Charging area determining and power enhancement method for multiexcitation unit configuration of wirelessly dynamic charging EV system," *IEEE Trans. Ind. Electron.*, vol. 66, no. 5, pp. 4086–4096, May 2019.

[12] Z. H. Wang, Y. P. Li, Y. Sun, C. S. Tang, and X. Lv, "Load detection model of voltage-fed inductive power transfer system," *IEEE Trans. Power Electron.*, vol. 28, no. 11, pp. 5233–5243, Nov. 2013.

[13] F. Zhang, S. A. Hackworth, W. Fu, C. Li, Z. Mao, and M. Sun, "Relay effect of wireless power transfer using strongly coupled magnetic resonances," *IEEE Trans. Magn.*, vol. 47, no. 5, pp. 1478–1481, May 2011.

[14] B. Luo, S. Wu, and Z. Nm, "Flexible design method for multi-repeater wireless power transfer system based on coupled resonator bandpass filter model," *IEEE Trans. Circuits Syst. I Regular Papers*, vol. 61, no. 11, pp. 3288–3297, Nov. 2014.

[15] S. Y. R. Hui, W. Zhong, and C. K. Lee, "A critical review of recent progress in mid-range wireless power transfer," *IEEE Trans. Power Electron.*, vol. 29, no. 9, pp. 4500–4511, Sep. 2014.

[16] C. K. Lee, W. X. Zhong, and S. Y. R. Hui, "Effects of magnetic coupling of nonadjacent resonators on wireless power domino-resonator systems," *IEEE Trans. Power Electron.*, vol. 27, no. 4, pp. 1905–1916, Apr. 2012.

[17] D. Ahn and S. Hong, "A study on magnetic field repeater in wireless power transfer," *IEEE Trans. Ind. Electron.*, vol. 61, no. 1, pp. 360–371, Jan. 2013.

[18] Z. Dong, S. Liu, X. Li, Z. Xu, and L. Yang, "A novel long-distance wireless power transfer system with constant current output based on domino-resonator," *IEEE J. Emerg. Sel. Topics Power Electron.*, vol. 9, no. 2, pp. 2343–2355, 2020.

[19] W. X. Zhong, C. K. Lee, and S. Y. Hui, "Wireless power domino-resonator systems with noncoaxial axes and circular structures," *IEEE Trans. Power Electron.*, vol. 27, no. 11, pp. 4750–4762, Nov. 2012.

[20] Z. Wenxing, K. L. Chi, and S. Y. Ron Hui, "General analysis on the use of tesla's resonators in domino forms for wireless power transfer," *IEEE Trans. Ind. Electron.*, vol. 60, no. 1, pp. 261–270, Jan. 2013.

[21] J. Lee and K. Lee, "Effects of number of relays on achievable efficiency of magnetic resonant wireless power transfer," *IEEE Trans. Power Electron.*, vol. 35, no. 7, pp. 6697–6700, Jul. 2020.

[22] J. Lee, K. Lee, and D. Cho, "Stability improvement of transmission efficiency based on a relay resonator in a wireless power transfer system," *IEEE Trans. Power Electron.*, vol. 32, no. 5, pp. 3297–3300, May 2017.

[23] J. Yin, D. Lin, C. K. Lee, and S. Y. Hui, "Monitoring of multiple loads in wireless power transfer systems without direct output feedback," in *Proc. IEEE Appl. Power Electron. Conf. Expo.*, 2014, pp. 1165–1170.

[24] J. Yin, D. Lin, C. K. Lee, and S. R. Hui, "Load monitoring and output power control of a wireless power transfer system without any wireless communication feedback," in *Proc. IEEE Energy Convers. Congr. Expo.*, 2013, pp. 4934–4939.

[25] W. Zhong and S. Hui, "Auxiliary circuits for power flow control in multifrequency wireless power transfer systems with multiple receivers," *IEEE Trans. Power Electron.*, vol. 30, no. 10, pp. 5902–5910, Oct. 2015.

[26] J. Qu, L. He, N. Tang, and L. Chi, "Wireless power transfer using domino-resonator for 110-kV power grid online monitoring equipment," *IEEE Trans. Power Electron.*, vol. 35, no. 11, pp. 11380–11390, Nov. 2020.

[27] C. Cheng *et al.*, "Load-Independent wireless power transfer system for multiple loads over a long distance," *IEEE Trans. Power Electron.*, vol. 34, no. 9, pp. 9279–9288, Sep. 2018.

Jinde Wu received the B.S. degree from the College of Information Engineering, Taiyuan University of Technology, Taiyuan, China, in 2015. He is currently working toward the Ph.D. degree in control theory and control engineering with Chongqing University, Chongqing, China.

His research interests include the bidirectional wireless power transfer and power electronics.

Xin Dai (Member, IEEE) received the B.S. degree in industrial automation from Yuzhou University, Chongqing, China, in 2000, and the Ph.D. degree in control theory and control engineering from the School of Automation, Chongqing University, Chongqing, China, in 2006.

In 2012, he was a Visiting Scholar with The University of Auckland, Auckland, New Zealand. He is currently working as a Professor with the School of Automation, Chongqing University. His research interests include inductive power transfer technology and nonlinear dynamic behavior analysis of power electronics.

Yue Sun (Member, IEEE) received the B.E. degree in electrical engineering, the M.E. degree in industry automation, and the Ph.D. degree in mechanical electrical integrated manufacturing from Chongqing University, Chongqing, China, in 1982, 1988, and 1995, respectively.

In 1997, he was a Senior Visiting Scholar with the University of Valenciennes, Valenciennes, France. He is currently a Professor with the School of Automation, Chongqing University. His research interests include automatic control, wireless power transfer, and power electronics applications.

Yanling Li received the Ph.D. degree from the School of Automation, Chongqing University, Chongqing, China, in 2017.

She is currently working with the School of Electrical Engineering and Electronics Information, Xihua University, Chengdu, China. Her research interests include wireless power transfer and advanced control technology in power electronics.